nature chemistry

Article

https://doi.org/10.1038/s41557-023-01367-y

A general strategy to develop fluorogenic polymethine dyes for bioimaging

Received: 6 February 2023

Accepted: 12 October 2023

Published online: 27 November 2023

Check for updates

Annabell Martin [1,2] & Pablo Rivera-Fuentes [1]

Fluorescence imaging is an invaluable tool to study biological processes and further progress depends on the development of advanced fluorogenic probes that reach intracellular targets and label them with high specificity. Excellent fluorogenic rhodamine dyes have been reported, but they often require long and low-yielding syntheses, and are spectrally limited to the visible range. Here we present a general strategy to transform polymethine compounds into fluorogenic dyes using an intramolecular ring-closure approach. We illustrate the generality of this method by creating both spontaneously blinking and no-wash, turn-on polymethine dyes with emissions across the visible and near-infrared spectrum. These probes are compatible with self-labelling proteins and small-molecule targeting ligands, and can be combined with rhodamine-based dyes for multicolour and fluorescence lifetime multiplexing imaging. This strategy provides access to bright, fluorogenic dyes that emit at wavelengths that are more red-shifted compared with those of existing rhodamine-based dyes.

Fluorescence microscopy is crucial to study the structure and function of cells. Fluorescent protein tags allow for the dynamic observation of proteins in living cells, but their brightness and photostability are often inferior to those of small-molecule fluorophores[1]. Fluorogenic dyes conjugated to self-labelling protein tags such as HaloTag[2] or SNAP-tag[3] combine the excellent photophysical properties of small-molecule dyes with the precise labelling of genetically encoded tags and have been widely used for fluorescence microscopy and nanoscopy.

The development of fluorogenic probes has predominantly focused on rhodamine-based scaffolds[4,5]. Rhodamine dyes exist in an equilibrium between a fluorescent zwitterionic (open) and a non-fluorescent spirocyclic (closed) form. This equilibrium is sensitive to the microenvironment of the probe. In media of low polarity and high pH, rhodamines are primarily present in the closed form, whereas polar media and low pH favour the open form[6–8]. Rhodamine dyes have been systematically optimized for fluorogenicity by varying the electron density of their conjugated core and by modulating the electronic character of the intramolecular nucleophile that closes the spirocycle[9,10]. These dyes, which span the visible range, display substantial fluorescence increase upon target binding and have been used for no-wash, multicolour, live-cell fluorescence imaging experiments. In contrast, the development of novel rhodamines with excitation and emission wavelengths in the near-infrared region (>700 nm) has been hampered by their complicated, long and low-yielding syntheses, as well as by their tendency to remain in the non-fluorescent form even upon binding to their target[11].

Polymethine dyes are some of the most used fluorophores in cell, tissue and whole-organism imaging due to their simple and highly modular synthesis, high extinction coefficients, biocompatibility, and tunable emission wavelengths spanning from the green to the shortwave infrared wavelengths. Members of this class of fluorophores include indoleninium-based dyes such as carbocyanines (Cy)[12–15] and squaraines[16–18], flavylium-based dyes[19,20], and coumarin–hemicyanine hybrid scaffolds[21–24], among others. The variety of applications of these dyes is illustrated by two classic examples: Indocyanine Green[25], a clinically approved, near-infrared dye for optical imaging of the vasculature, and Cy5 derivatives (for example, AlexaFluor 647), which are the most widely used fluorophores in single-molecule localization microscopy (SMLM)[26]. Many elegant turn-on mechanisms for polymethine dyes have been reported.[27–30] However, so far there is no reported general strategy to impart binding-induced fluorogenicity to polymethine

[1]Department of Chemistry, University of Zurich, Zurich, Switzerland. [2]École Polytechnique Fédérale de Lausanne (EPFL), Institute of Chemical Sciences and Engineering, Lausanne, Switzerland. e-mail: pablo.riverafuentes@uzh.ch

https://doi.org/10.1038/s41557-023-01367-y

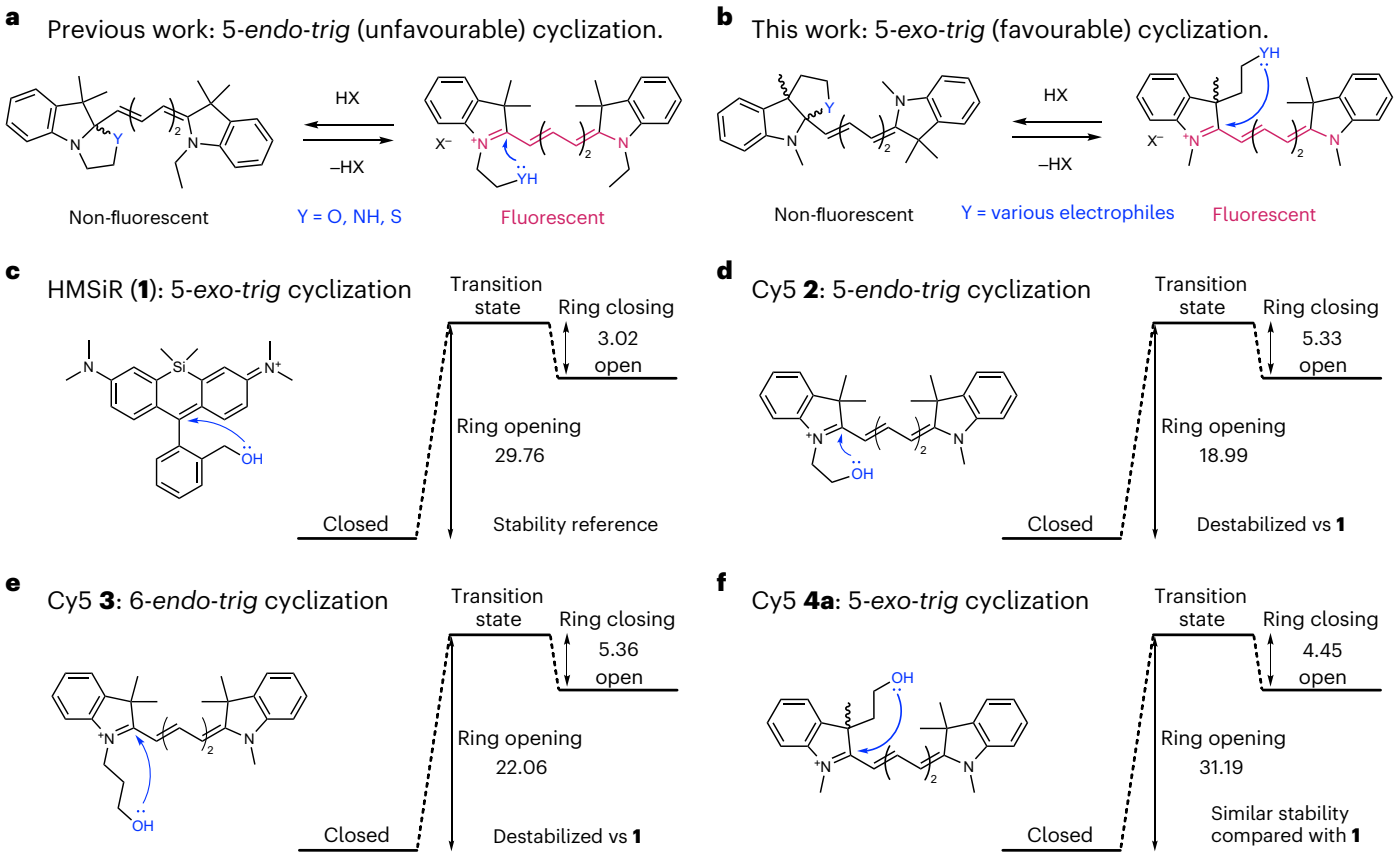

Fig. 1 | Intramolecular cyclization reactions of carbocyanines and HMSiR (1). **a**, Example of previous work using a 5-*endo-trig* cyclization to create fluorogenic carbocyanine dyes[31–34]. **b**, 5-*exo-trig* cyclization as a robust and general strategy towards fluorogenicity in polymethine dyes. **c**–**f**, Structures and calculated energies of ring opening and closing of rhodamine HMSiR (**1**) (**c**), and Cy5 derivatives **2** (**d**), **3** (**e**) and **4a** (**f**). Energies (kcal mol^{-1}) were calculated at the B3LYP/DGTZVP level of theory. A summary of calculated energies using the B3LYP or M06-2X functional can be found in Supplementary Table 1.

dyes and thus their applicability in live-cell imaging of specific protein targets remains very limited.

Unlike rhodamine-based dyes, polymethine fluorophores do not possess a built-in intramolecular cyclization equilibrium that could be leveraged to induce fluorogenicity; however, the addition of nucleophilic side chains has been used as a strategy to create fluorogenic polymethine dyes. For instance, Cy5 and Cy7 dyes have been decorated with alcohols, amines and thiols as nucleophiles, thereby forming oxazines, diazines and thiazines, respectively[31–34]. Coumarin–hemicyanine hybrid fluorophores have been generated with a *p*-nitrophenol group that exists mainly in the spirocyclic form but can undergo a photoinduced and reversible interconversion into its open fluorescent form[24]. Furthermore, coumarin–hemicyanine hybrid fluorophores have been developed with a hydroxyethyl ring-closing moiety to generate esterase-activatable fluorescent probes[21]. Despite these efforts, cyclization reactions in polymethine dyes have not been as efficient as in rhodamines, and the creation of robustly fluorogenic polymethine dyes has so far remained elusive. In this work we applied classic organic chemistry heuristics to design favourable cyclization reactions that led to a general strategy for the creation of fluorogenic polymethine dyes for live-cell imaging.

Results and discussion

Probe design and validation

An efficient fluorogenic dye must exist exclusively in the non-fluorescent form unless it is bound to its intended target. In the case of cyclization-based fluorogenicity, it means that the barrier of ring opening and closure must be high and low, respectively (Extended Data Fig. 1). The favourability of polar cyclization reactions can be estimated using heuristic guidelines known as the Baldwin rules (Extended Data Fig. 1)[35]. We noticed that in past attempts to create fluorogenic polymethine dyes, the intramolecular cyclization was of the 5-*endo-trig* type, which is unfavourable according to the Baldwin rules (Extended Data Fig. 1). This cyclization (Fig. 1a) is classified as 5-*endo-trig* because it involves the formation of a five-membered ring that contains (*endo*) the single bond formed from the double bond of the trigonal (*trig*) carbon attacked by the nucleophile (Fig. 1a). Although 6-*endo-trig* cyclizations should be more favourable than 5-*endo-trig*, past attempts at using 6-*endo-trig* cyclizations to impart fluorogenicity did not lead to more stable cyclic isomers[31–34]. Based on these observations, we hypothesized that a 5-*exo-trig* cyclization—in which the single bond that forms upon attack of the double bond is not contained (*exo*) within the newly formed ring (Fig. 1b)—would be a more efficient alternative.

To test our hypothesis, we used density functional theory (DFT) to calculate the energies of ring opening and closure for HMSiR (**1**)—a silicon rhodamine derivative with an efficient 5-*exo-trig* intramolecular cyclization reaction (Fig. 1c)[36]. We then compared these values with those calculated for Cy5 derivatives **2, 3** and **4a**, which undergo 5-*endo-trig*, 6-*endo-trig* and 5-*exo-trig* cyclizations, respectively (Fig. 1d–f). HMSiR (**1**) has larger ring-opening and smaller ring-closing energies than Cy5 derivatives **2** and **3**, which undergo 5- and 6-*endo-trig* cyclizations, respectively (Fig. 1c,d). In contrast, the energies of ring opening and closure in Cy5 derivative **4a**—which undergoes a 5-*exo-trig* cyclization—compare favourably with the computed values for HMSiR (**1**) (Fig. 1c,f). We also observed that judicious addition of electron-withdrawing groups to the Cy5 dye further increased the stability of the closed isomer (for example, derivative **4b**; Extended Data Fig. 1), allowing for additional modulation of the energies of ring

opening and closure. These predictions suggested that more robust fluorogenic polymethine dyes could be obtained simply by employing a 5-*exo-trig* cyclization instead of a 5-*endo-trig* one.

To test these computational predictions, we prepared the indoleninium building blocks **5, 6, 7a**–**d** and linker **8** (Fig. 2a and Supplementary Information) according to published procedures[37–40]. We next synthesized the 5-*endo-trig* Cy5 probes **2a** and **2b** in a two-step, microwave-assisted procedure (Supplementary Information). The 5-*exo-trig* Cy5 probes **4a** and **4b** were prepared in two steps via methyl ester intermediates **9a**–**d**, followed by reduction with $LiAlH_4$ (Fig. 2a). We performed pH titrations of these Cy5 derivatives to evaluate the stability of the closed isomer (Fig. 2b and Supplementary Fig. 1). The pH titrations of 5-*endo-trig* probes revealed ring-opening pK_a values above physiological pH (11.1 for **2a** and 8.5 for **2b**), indicating that these probes would be highly fluorescent as free small molecules in cells. By contrast, the ring-opening pK_a values of 5-*exo-trig* probes were below 7 (6.4 for **4a** and 5.7 for **4b**), suggesting that they might only show some fluorescence in acidic compartments. Furthermore, 5-*exo-trig* compounds **4a** and **4b** have a much higher propensity to cyclize in medium of low dielectric constant than their 5-*endo-trig* counterparts **2a** and **2b** (Supplementary Fig. 2).

In live-cell imaging experiments (Fig. 2c), the 5-*endo-trig* probes **2a** and **2b** exhibited bright fluorescence in mitochondria (Fig. 2c and Extended Data Fig. 2). This subcellular localization is probably a consequence of the delocalized positive charge of the open Cy5 scaffold. By contrast, 5-*exo-trig* probes **4a** and **4b** exhibited only very faint fluorescence, which was mostly localized in the lysosomes (Fig. 2c and Extended Data Fig. 2). These results confirm that the closed form of the probes that undergo 5-*exo-trig* cyclizations (**4a** and **4b**) is very stable under physiological conditions and greatly minimizes non-specific background in live-cell imaging.

We next investigated whether we could induce fluorescence turn-on upon conjugation of dye **4b** to a self-labelling protein tag. Given that HaloTag has been thoroughly optimized for rhodamine-based dyes[2,41], we chose to work with SNAP-tag[42], thereby providing an orthogonal system that could be used in multiplexing studies with rhodamines and HaloTag. We synthesized the azide-modified SNAP-tag ligand **10** using the diazotizing reagent FSO_2N_3 (ref. 43) and combined it with alkyne-modified Cy5 dye **4c** in a click reaction to generate probe **11** (Fig. 2d and Methods). This dye displayed a 10-fold turn-on in absorbance and a 21-fold turn-on in fluorescence when incubated with purified SNAP-tag protein (Fig. 2e and Methods), demonstrating its fluorogenicity upon binding to a self-labelling tag. Live-cell experiments using SNAP-tag fused to a fragment of histone H2B demonstrated that although the cellular uptake of compound **11** is not enhanced compared to its 5-*endo-trig* derivative, it labels SNAP-tag more efficiently and display much less non-specific signal (Supplementary Fig. 3).

Importantly, probe **11** was designed to mimic the cyclization equilibrium in HMSiR (**1**), which is a spontaneously blinking fluorophore useful for SMLM. Thus, to assess the spontaneous blinking properties of probe **11**, we expressed SNAP-tag fused to β-tubulin in HeLa cells and treated these cells with compound **11** (Methods and Supplementary Tables 2 and 3). We performed live-cell SMLM imaging in growth medium without any blinking or anti-fading agents. These experiments revealed that probe **11** indeed displays spontaneous blinking, allowing for the acquisition of super-resolved fluorescence images (Fig. 2f). Single molecules of probe **11** could be localized with a precision of 18 ± 6 (mean ± s.d.) nm, and widths of about 60 nm were measured for microtubules in living cells (Fig. 2f). These results are comparable to those obtained with HMSiR (**1**)[36].

A fluorogenic Cy5 derivative

We next applied the 5-*exo-trig* ring-closing strategy to develop a no-wash, fluorogenic Cy5 derivative. After synthesizing a few derivatives and testing the effect of pH and polarity on their cyclization equilibrium (Supplementary Discussion 1), we transformed the methyl ester group of **9c** into *N*-methyl amide **12** and prepared the corresponding 5-*endo-trig* indoleninium **13** and Cy5 probe **14** (Fig. 3a). These alkyne-bearing derivatives were conjugated to benzyl guanine **10** to generate probes **15** and **16** (Fig. 3b). Incubation of these dyes with purified SNAP-tag protein led to a 6-fold increase in absorbance and 19-fold increase in fluorescence for compound **15**. The larger turn-on in fluorescence indicates that binding to SNAP-tag not only induces ring opening but also increases the quantum yield of emission of compound **15** compared with the free dye in solution (Supplementary Table 4). In comparison, compound **16** underwent only a 1.4-fold and 2.5-fold increase in absorbance and fluorescence, respectively, upon binding to SNAP-tag (Fig. 3c). The in vitro fluorogenicity of probe **15** is comparable with that of the popular JF646 dye functionalized with a benzyl guanine (JF646-BG) for SNAP-tag labelling (Fig. 3c). This observation confirms that the 5-*exo-trig* cyclization of polymethine dyes can be reversed upon binding to protein targets, analogously to the turn-on mechanism of rhodamines.

We then performed no-wash, live-cell imaging to compare the performance of probes **15**, **16** and JF646. We transfected HeLa cells with a plasmid that encodes the fusion protein H2B-SNAPf-mTurquoise2 and incubated them with dyes **15, 16** or JF646-BG (Fig. 3d). Probe **15** exhibited bright fluorescence signal in the nucleus and only very faint unspecific background signals. This performance was comparable with that of JF646-BG (Fig. 3d). Probe **16**, on the other hand, displayed a >10-fold-weaker fluorescence signal, indicating that it might be less membrane-permeant (Fig. 3d). Furthermore, probe **16** exhibited most of its fluorescent signal in vesicles, confirming that 5-*endo-trig* Cy5 derivatives are not suitable as no-wash turn-on dyes. Finally, we tested the generality of labelling with probe **15** by transfecting HeLa cells with plasmids encoding for an untargeted SNAPf-mTurquoise2 fusion protein (whole cell), LifeAct-SNAPf-mTurquoise2 (actin) or TOM20-SNAPf-mTurquoise2 (mitochondria). In all cases, labelling was specific, as judged by the excellent overlay between the signal of the reference fluorescent protein mTurquoise2 and that of **15** linked to SNAP-tag (Fig. 3d).

The 5-*exo-trig* ring-closure design leads to an indolenine fragment that contains a chiral carbon (Extended Data Fig. 3). To investigate the effect of stereochemistry on the ring opening of the dye upon binding to SNAP-tag, we separated the enantiomers of **6**, (+)-**6** and (−)-**6** using a chiral stationary phase. We employed electronic circular dichroism and time-dependent density functional theory (TD-DFT)[44] to assign the absolute configuration of the two enantiomers (Extended Data

Fig. 2 | Synthesis and imaging properties of 5-*endo-trig* and 5-*exo-trig* Cy5 derivatives. a, Synthesis of 5-*endo*-trig and 5-*exo-trig* Cy5 dyes with a hydroxy group as a ring-closing moiety. **b**, The pH profiles of dyes **2a, 2b, 4a** and **4b**. Symbols indicate the mean of three independent experiments and error bars represent the s.d. **c**, Intracellular fluorescence of untargeted 5-*endo-trig* (**2a,b**) and 5-*exo-trig* Cy5 derivatives (**4a,b**) in HeLa cells. The calibration bar indicates raw pixel values. Micrographs are representative of three independent biological samples measured over three separate imaging sessions. **d**, SNAP-tag functionalization of **4c** to yield SNAP-tag-reactive probe **11**. **e**, Protein-binding turn-on of **11** (2.5 μM) incubated with purified SNAP-tag protein (5 μM) in phosphate-buffered saline (PBS) for 1.5 h. The lines indicate absorbance (solid) or fluorescence (dotted) of the free dye in solution (grey) or the dye–protein conjugate (red). Spectra are the mean from three independent experiments. **f**, Single-molecule localization microscopy imaging of **11** (100 nM) in live HeLa cells transfected with β-tubulin-SNAP-tag. A comparison between a super-resolved and a diffraction-limited image (upper left), and localization precision of single-molecules of probe **11** in live cells is also shown (bottom left). Scale bar, 20 μm (**c**) and 2 μm (**f**). Data are representative of three independent experiments performed in three different imaging sessions. FWHM, full-width at half-maximum.

https://doi.org/10.1038/s41557-023-01367-y

Fig. 3 and Methods), and found that (−)-**6** has *S* absolute configuration ((+)-(*R*)-**6** and (−)-(*S*)-**6**). We used each enantiomer separately to prepare enantiomerically pure probes (*R*)-**15** and (*S*)-**15**. We did not observe a substantial difference in fluorogenicity upon binding of each enantiomer to either purified SNAP-tag or in live-cell imaging (Extended Data Fig. 3). We hypothesize that the relatively long distance between the chiral centre of the dye and the protein surface alleviates any potential enantioselective binding interactions; however,

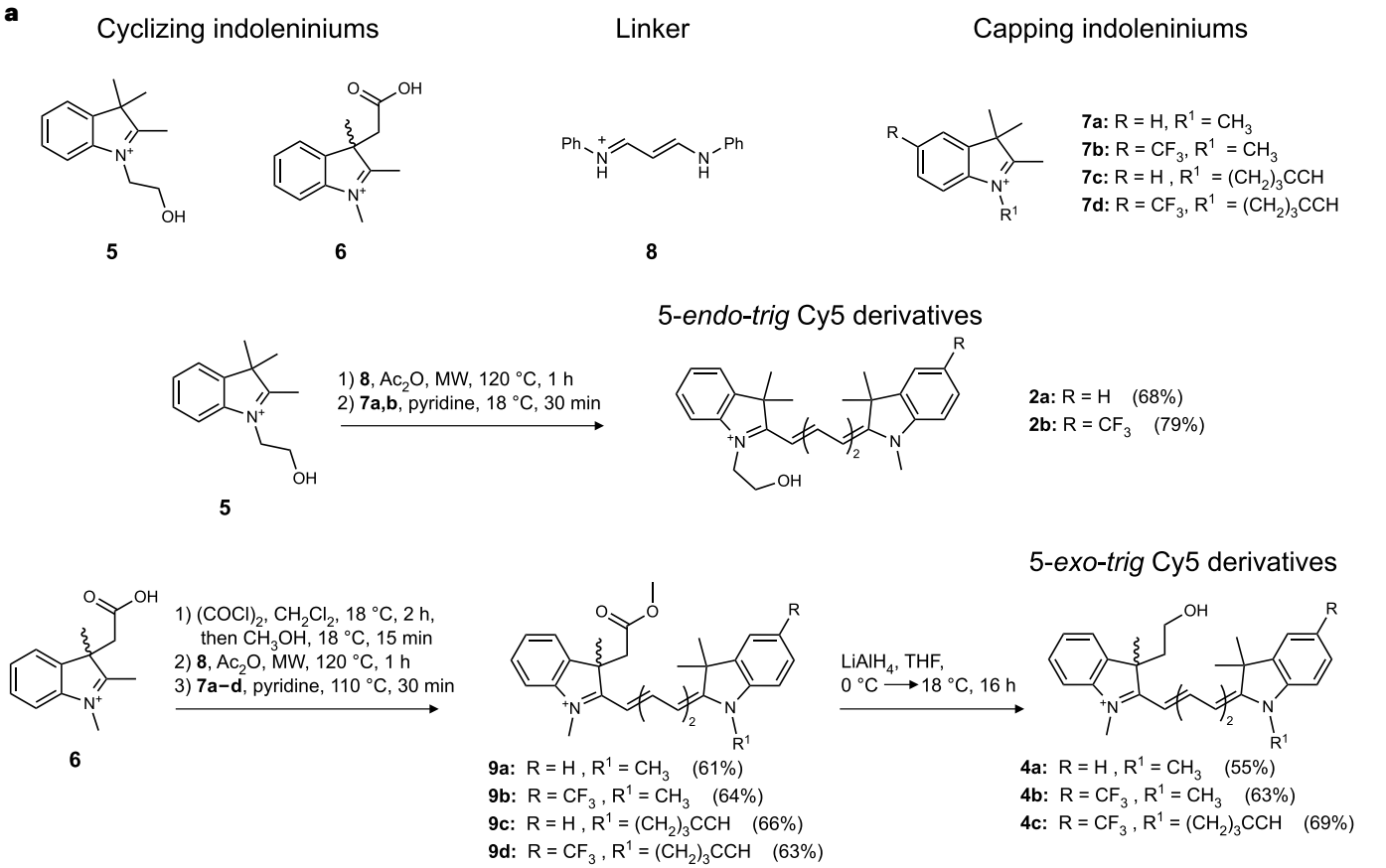

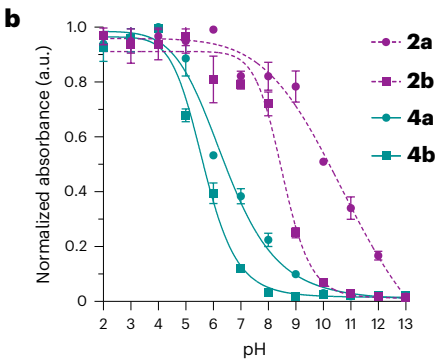

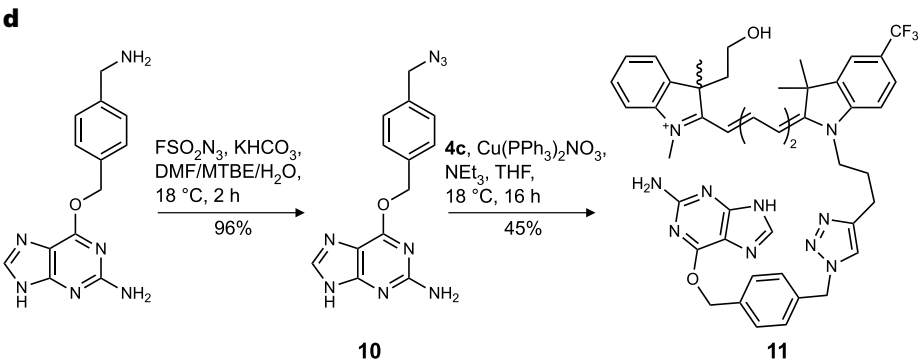

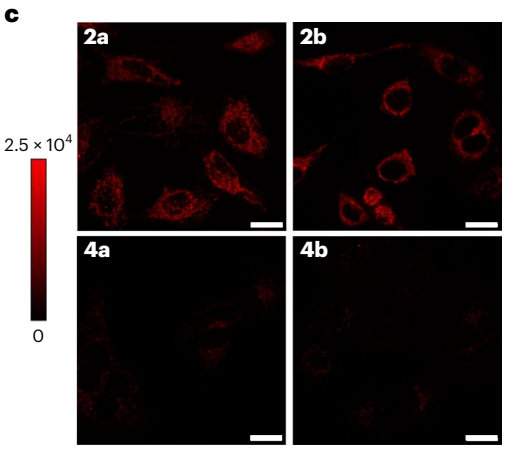

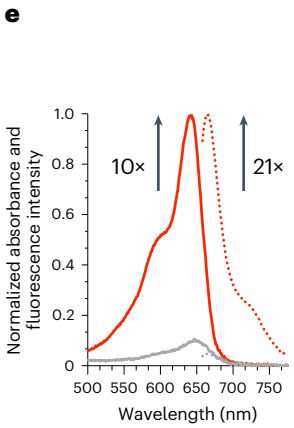

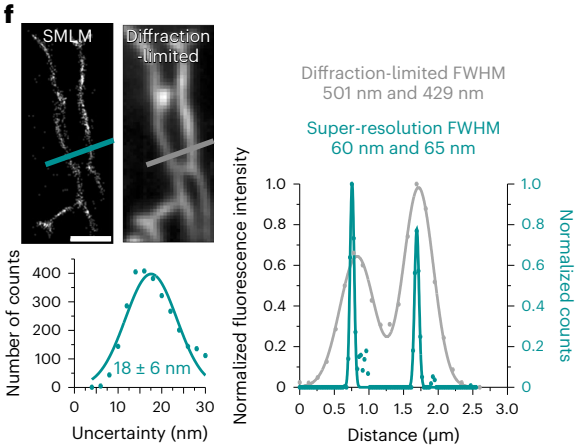

https://doi.org/10.1038/s41557-023-01367-y

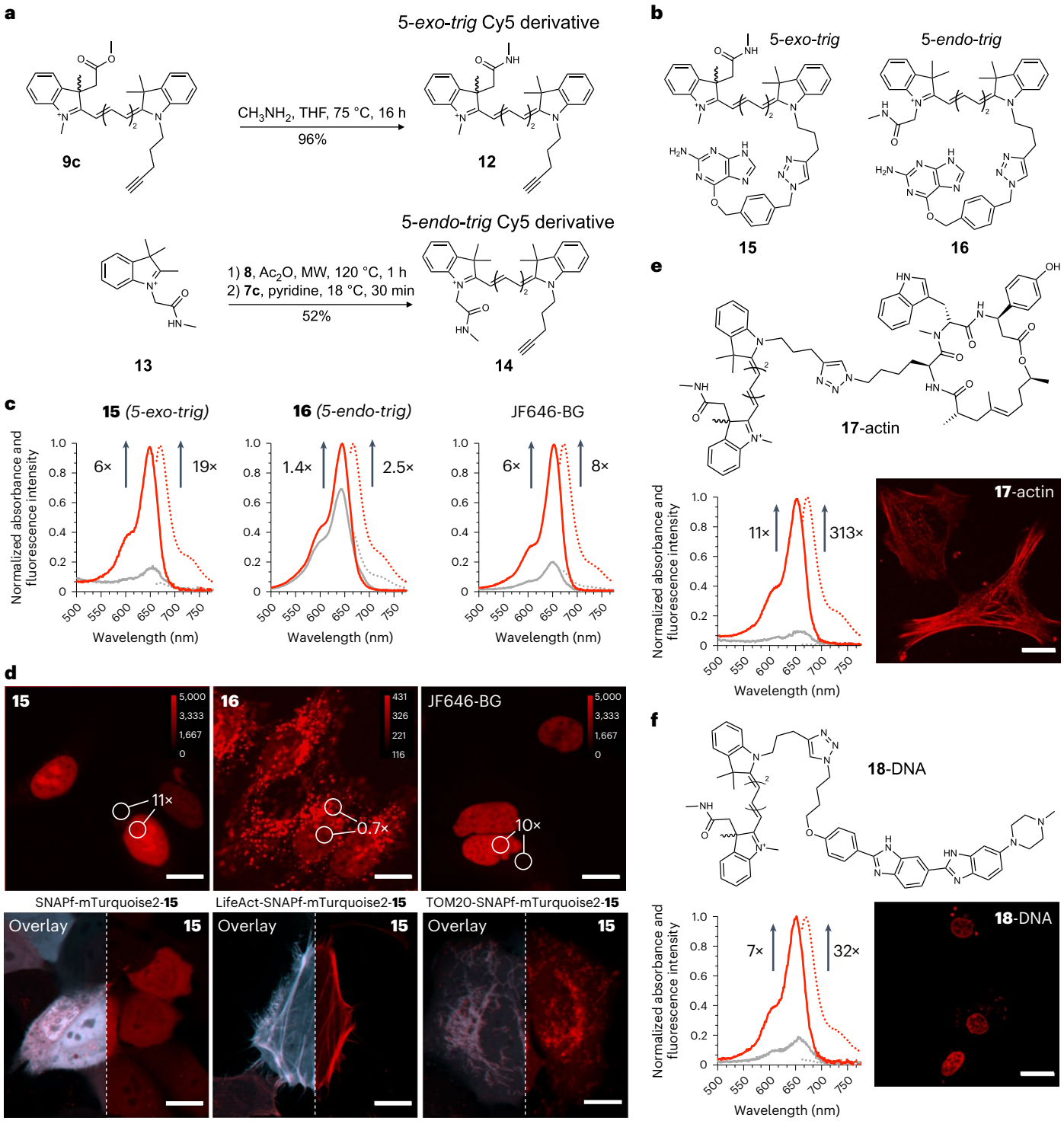

Fig. 3 | Synthesis, in vitro evaluation and live-cell validation of fluorogenic Cy5 derivatives. a, Synthesis of 5-*exo-trig* and 5-*endo-trig* Cy5 derivatives with an *N*-methyl amide as a ring-closing moiety. **b**, Structures of compounds **15** and **16** functionalized with benzyl guanine for SNAP-tag labelling. **c**, Protein-binding turn-on of **15, 16** or JF646-BG with SNAP-tag protein. For protein-binding studies, probes (2.5 µM) were incubated with 5 µM purified SNAP-tag protein in PBS for 1.5 h at pH 7.4. **d**, No-wash, live-cell imaging of HeLa cells that were transfected with H2B-SNAPf-mTurquoise2 (upper images) or with the indicated plasmid (lower images) and incubated with **15** (50 nM), **16** (50 nM) or JF646-BG (50 nM) as indicated. The calibration bars indicate raw pixel values. **e**, Structure, protein-binding turn-on and no-wash live-cell imaging in HeLa cells of **17**-actin. The concentration of **17**-actin was 2.5 µM for protein-binding studies and 250 nM for cell imaging. **f**, Structure, DNA-binding turn-on and live-cell imaging in HeLa cells of **18**-DNA. The concentration of **18**-DNA was 1 µM for DNA-binding studies and 500 nM for cell imaging. Scale bars, 15 µm. Spectra are the mean from three independent experiments and the lines indicate absorbance (solid) or fluorescence (dotted) of the free dye in solution (grey) or the dye–macromolecule conjugate. Micrographs are representative of three independent biological samples measured over three separate imaging sessions.

https://doi.org/10.1038/s41557-023-01367-y

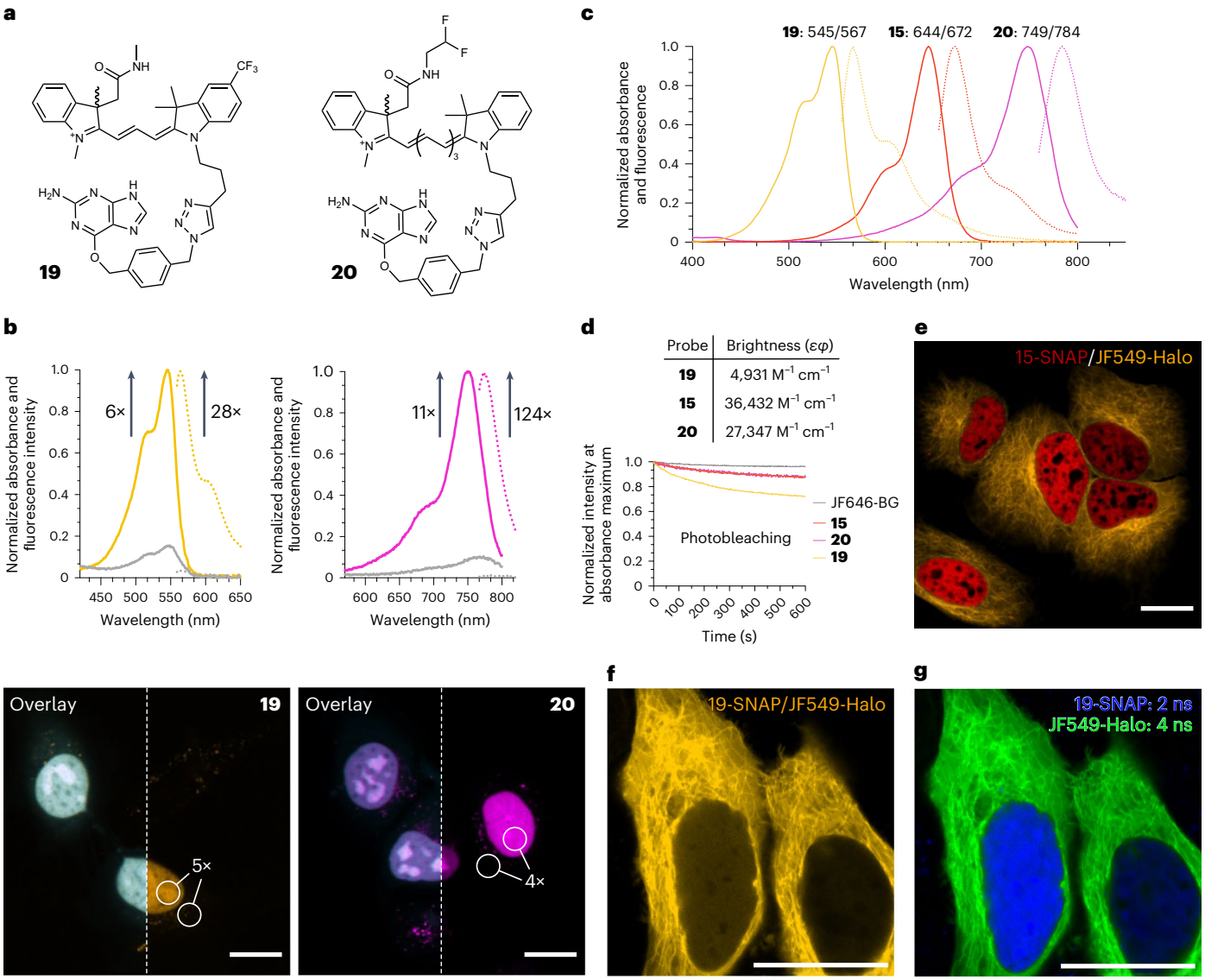

Fig. 4 | Synthesis, in vitro evaluation and live-cell validation of fluorogenic Cy3 and Cy7 derivatives. a, Structures of Cy3 and Cy7 derivatives **19** and **20**. **b**, SNAP-tag-binding turn-on and no-wash live-cell imaging of HeLa cells transfected with H2B-SNAPf-mTurquoise2 and treated with **19** (50 nM) or **20** (250 nM). The lines indicate absorbance (solid) or fluorescence (dotted) of the free dye in solution (grey) or the dye–protein conjugate (coloured). Spectra are the mean from three independent experiments. Scale bars, 15 µm. **c**, Normalized absorbance and fluorescence spectra of Cy3 **19**, Cy5 **15** and Cy7 **20** measured in ethanol + 0.1% TFA. Spectra represent single measurements. **d**, Brightness of SNAP-tag adducts in PBS, pH 7.4 and photobleaching curves measured for SNAP-tag adducts at a concentration of 50 nM in PBS following irradiation at the maximum excitation wavelength with monochromatic light (1.2 mW power). Photobleaching curves represent the mean from three independent experiments. **e**, Multicolour no-wash imaging in live HeLa cells co-transfected with H2B-SNAPf-mTurquoise2 and TUBB5-Halo, and incubated with **15** (50 nM) and **JF549**-Halo (50 nM). Scale bar, 15 µm. **f**, Total intensity measured in a cell co-transfected with H2B-SNAPf-mTurquoise2 and TUBB5-Halo and incubated with **19** (50 nM) and **JF549**-Halo (10 nM). Scale bar, 20 µm. **g**, Fluorescence lifetime multiplexing of the cell shown in **f**. Scale bar, 20 µm. All micrographs are representative of three independent biological samples measured over three separate imaging sessions.

we argue that such interactions could be leveraged to further increase the fluorogenicity of 5-*exo-trig* polymethine probes upon binding to chiral targets.

We next tested whether binding to other macromolecular targets also induced fluorescence turn-on in probe **15**. For this purpose, we prepared compounds **17**-actin and **18**-DNA. These probes were composed of a 5-*exo-trig* Cy5 derivative linked through a triazole-containing alkane to either the actin-binding cyclo-depsipeptide jasplakinolide (Fig. 3e)[45,46] or to Hoechst 33342 (Fig. 3f)—a dye that binds to the minor groove of double-stranded DNA (dsDNA) and has been used to target fluorogenic rhodamine dyes to the cell nucleus[47]. Probe **17**-actin showed fluorogenic behaviour with an 11-fold turn-on in absorbance and 313-fold turn-on in fluorescence upon binding to actin filaments in vitro (Fig. 3e). The much larger fluorescence turn-on compared to absorbance increase indicates that binding to actin considerably enhances the quantum yield of carbocyanine **17**. In live-cell imaging experiments, **17**-actin labelled actin fibres selectively in live, unmodified HeLa cells. Similar results were obtained for **18**-DNA, which displayed a 7-fold increase in absorbance and 32-fold increase in fluorescence upon binding to double-stranded DNA (Fig. 3f). Live-cell imaging also confirmed specific staining of the cell nucleus (Fig. 3f). These results demonstrate that the fluorogenicity of 5-*exo-trig* Cy5 derivatives is not limited to SNAP-tag, and other macromolecules can also induce fluorescence turn-on.

Fluorogenic Cy3 and Cy7 derivatives

Carbocyanine dyes can cover a large spectral range by varying the number of conjugated carbon atoms in between the two indoleninium moieties. We therefore explored whether the 5-*exo-trig* fluorogenic strategy could be extended to Cy3 and Cy7 dyes, providing fluorophores for two extra imaging channels. We suspected that the Cy3 derivative would have a higher LUMO energy than Cy5, whereas the opposite would be true for the Cy7 derivative; thus, we expected the Cy3 dyes to be more likely to adopt the open form than Cy5 dyes, whereas Cy7 dyes would tend to adopt the closed form. To balance these trends, we added a CF_3 moiety on the capping indoleninium to favour the closed form of Cy3. Similarly, we replaced the nucleophilic *N*-methyl amide with an electron-deficient amide to facilitate ring-opening in our Cy7 design. From a synthetic point of view, compared with the preparation of Cy5 derivatives, we only changed the commercially available linker and adjusted the temperatures during the microwave-assisted protocol (Supplementary Information).

We prepared Cy3 derivative **19** and Cy7 derivative **20** (Fig. 4a) for SNAP-tag labelling. Both probes displayed fluorogenic behaviour upon binding to purified SNAP-tag protein, with increases in absorbance of 6-fold for **19** and 11-fold for **20**, and increases in fluorescence of 28-fold for **19** and 124-fold for **20** (Fig. 4b). Similar to compound **15**, the large turn-on in fluorescence indicates that binding to SNAP-tag considerably increases the quantum yield of emission of these probes compared with the free dyes in solution (Supplementary Table 4). Probes **19** and **20** were then used in no-wash live-cell imaging experiments with HeLa cells transiently transfected with the H2B-SNAPf-mTurquoise2 plasmid described before. We observed excellent co-localization of the mTurquoise2 reference signal with the yellow and near-infrared fluorescence signals of **19** and **20**, respectively, confirming the specificity of the probes (Fig. 4b). Labelling of other cellular structures was performed with similar results (Extended Data Fig. 4). Probes **15**, **19** and **20** cover a substantial portion of the visible spectrum and reach into the near-infrared region. Probes **15** and **20** display excellent brightness and good photostability when bound to SNAP-tag (Fig. 4c,d, Supplementary Table 4, and Supplementary Fig. 4 and 5). Cy3 derivative **19** is not as bright or photostable, but these properties could be further tuned by introducing substituents or by making the polymethine chain more rigid[48].

Finally, we applied our probes to multiplexing experiments. First, we performed multicolour imaging experiments using the fluorogenic Cy5 dye **15** in combination with the widely used JF549-Halo dye. We confirmed the orthogonality of our fluorogenic probe with rhodamine-HaloTag conjugates by imaging the **15**/JF549-Halo pair in live HeLa cells co-transfected with H2B-SNAPf-mTurquoise2 and TUBB5-HaloTag (Fig. 4e). We next explored whether the fluorescence signals of the Cy3 derivative **19** and JF549-Halo—which have nearly identical excitation and emission wavelengths—could be separated by their excited-state lifetimes. We co-transfected HeLa cells with H2B-SNAPf-mTurquoise2 and TUBB5-HaloTag, and performed fluorescence lifetime imaging (FLIM). Although the signals could not be separated by their wavelength (Fig. 4f), they could be easily distinguished by their average excited-state lifetimes (2 ns for **19** and 4 ns for JF549-Halo, Fig. 4g) using phasor plot analysis.

Conclusion

We presented a general strategy to impart fluorogenicity to polymethine dyes via a 5-*exo-trig* ring-closure approach. These dyes, regardless of their excitation wavelength, can be readily synthesized in two high-yielding steps and are easy to derivatize by varying the indoleninium building blocks or the ring-closing moiety. We have illustrated the potential of our fluorogenic polymethine scaffold by generating a spontaneously blinking Cy5 dye, fluorogenic Cy3 and Cy5 dyes, and a bright and photostable near-infrared fluorogenic Cy7. Cy7 derivative probe **20** is particularly interesting due to its high brightness ($\varepsilon\varphi$: product of extinction coefficient and quantum yield) and long emission wavelength ($\varepsilon\phi$ = 27,300 M^{-1} cm^{-1} and λ_{em} = 784 nm), particularly when compared with fluorescent proteins in the same spectral range (for example, miRFP718nano, $\varepsilon\phi$ = 4,500 M^{-1} cm^{-1} and λ_{em} = 718 nm; ref. 49). Furthermore, we showed that these probes can be used for no-wash confocal live-cell microscopy and SMLM; it can also be used in combination with the widely used rhodamine-HaloTag conjugates in multicolour and multiplexed lifetime imaging experiments.

We demonstrated the versatility of our turn-on strategy by using the self-labelling protein tag SNAP-tag, as well as jasplakinolide or Hoechst 33342 dye, to drive fluorescence turn-on. The mechanism of fluorescence turn-on of 5-*exo-trig* to such varied macromolecular targets remains to be fully elucidated. Preliminary modelling results suggest that ring-opening could be triggered by specific interactions (for example, hydrogen bonds) between the lactam rings and ubiquitous amides in proteins or phosphate groups in nucleic acids (Supplementary Discussion 2). More detailed studies including molecular dynamics simulations and site-directed mutagenesis could shed further light on the mechanism of fluorescence turn-on for specific 5-*exo-trig* polymethine dyes.

Given the high modularity of polymethine dyes, the spectral range can be further extended into the green (for example, Cy1 dyes[50]) as well as into the shortwave infrared (for example, Cy9 dyes[51]) wavelengths. Furthermore, the photophysical properties and fluorogenicity of polymethine dyes could be further tuned by varying the substituents on the indolenines or the linker[13]. We envision that this simple, yet general, method will be used to develop improved fluorogenic probes, facilitating new bioimaging experiments.

Online content

Any methods, additional references, Nature Portfolio reporting summaries, source data, extended data, supplementary information, acknowledgements, peer review information; details of author contributions and competing interests; and statements of data and code availability are available at https://doi.org/10.1038/s41557-023-01367-y.

References

1. Grimm, J. B. & Lavis, L. D. Caveat fluorophore: an insiders' guide to small-molecule fluorescent labels. *Nat. Methods* **19**, 149–158 (2022).
2. Los, G. V. et al. HaloTag: a novel protein labeling technology for cell imaging and protein analysis. *ACS Chem. Biol.* **3**, 373–382 (2008).
3. Keppler, A. et al. A general method for the covalent labeling of fusion proteins with small molecules in vivo. *Nat. Biotechnol.* **21**, 86–89 (2003).
4. Lavis, L. D. Teaching old dyes new tricks: biological probes built from fluoresceins and rhodamines. *Annu. Rev. Biochem.* **86**, 825–843 (2017).
5. Wang, L., Frei, M. S., Salim, A. & Johnsson, K. Small-molecule fluorescent probes for live-cell super-resolution microscopy. *J. Am. Chem. Soc.* **141**, 2770–2781 (2018).
6. Urano, Y. et al. Evolution of fluorescein as a platform for finely tunable fluorescence probes. *J. Am. Chem. Soc.* **127**, 4888–4894 (2005).
7. Lukinavičius, G. et al. A near-infrared fluorophore for live-cell super-resolution microscopy of cellular proteins. *Nat. Chem.* **5**, 132–139 (2013).
8. Grimm, J. B. et al. A general method to improve fluorophores for live-cell and single-molecule microscopy. *Nat. Methods* **12**, 244–250 (2015).
9. Wang, L. et al. A general strategy to develop cell permeable and fluorogenic probes for multicolour nanoscopy. *Nat. Chem.* **12**, 165–172 (2020).
10. Grimm, J. B. et al. A general method to fine-tune fluorophores for live-cell and in vivo imaging. *Nat. Methods* **14**, 987–994 (2017).

11. Grimm, J. B. et al. A general method to optimize and functionalize red-shifted rhodamine dyes. *Nat. Methods* **17**, 815–821 (2020).
12. Gorka, A. P., Nani, R. R. & Schnermann, M. J. Harnessing cyanine reactivity for optical imaging and drug delivery. *Acc. Chem. Res.* **51**, 3226–3235 (2018).
13. Štacková, L., Štacko, P. & Klán, P. Approach to a substituted heptamethine cyanine chain by the ring opening of Zincke salts. *J. Am. Chem. Soc.* **141**, 7155–7162 (2019).
14. Altman, R. B. et al. Cyanine fluorophore derivatives with enhanced photostability. *Nat. Methods* **9**, 68–71 (2011).
15. Gidi, Y. et al. Unifying mechanism for thiol induced photoswitching and photostability of cyanine dyes. *J. Am. Chem. Soc.* **142**, 12681–12689 (2020).
16. Ros-Lis, J. V. et al. Squaraines as fluoro-chromogenic probes for thiol-containing compounds and their application to the detection of biorelevant thiols. *J. Am. Chem. Soc.* **126**, 4064–4065 (2004).
17. Ajayaghosh, A. Chemistry of squaraine-derived materials: near-IR dyes, low band gap systems, and cation sensors. *Acc. Chem. Res.* **38**, 449–459 (2005).
18. Karpenko, I. A. et al. Fluorogenic squaraine dimers with polarity-sensitive folding as bright far-red probes for background-free bioimaging. *J. Am. Chem. Soc.* **137**, 405–412 (2015).
19. Cosco, E. D. et al. Shortwave infrared polymethine fluorophores matched to excitation lasers enable non-invasive, multicolour in vivo imaging in real time. *Nat. Chem.* **12**, 1123–1130 (2020).
20. Cosco, E. D. et al. Bright chromenylium polymethine dyes enable fast, four-color in vivo imaging with shortwave infrared detection. *J. Am. Chem. Soc.* **143**, 6836–6846 (2021).
21. Fujioka, H. et al. Activatable fluorescent probes for hydrolase enzymes based on coumarin–hemicyanine hybrid fluorophores with large Stokes shifts. *Chem. Commun.* **56**, 5617–5620 (2020).
22. Wrobel, A. T., Johnstone, T. C., Liang, A. D., Lippard, S. J. & Rivera-Fuentes, P. A fast and selective near-infrared fluorescent sensor for multicolor imaging of biological nitroxyl (HNO). *J. Am. Chem. Soc.* **136**, 4697–4705 (2014).
23. Tirla, A. & Rivera-Fuentes, P. Development of a photoactivatable phosphine probe for induction of intracellular reductive stress with single-cell precision. *Angew. Chem. Int. Ed.* **55**, 14709–14712 (2016).
24. Deniz, E., Sortino, S. & Raymo, F. M. Fluorescence switching with a photochromic auxochrome. *J. Phys. Chem. Lett.* **1**, 3506–3509 (2010).
25. Alander, J. T. et al. A review of Indocyanine Green fluorescent imaging in surgery. *Int. J. Biomed. Imag.* **2012**, 1–26 (2012).
26. Lelek, M. et al. Single-molecule localization microscopy. *Nat. Rev. Methods Primer* **1**, 39 (2021).
27. Demeter, O. et al. Bisazide cyanine dyes as fluorogenic probes for bis-cyclooctynylated peptide tags and as fluorogenic cross-linkers of cyclooctynylated proteins. *Bioconjug. Chem.* **28**, 1552–1559 (2017).
28. Knorr, G. et al. Bioorthogonally applicable fluorogenic cyanine-tetrazines for no-wash super-resolution imaging. *Bioconjug. Chem.* **29**, 1312–1318 (2018).
29. Usama, S. M., Inagaki, F., Kobayashi, H. & Schnermann, M. J. Norcyanine-carbamates are versatile near-infrared fluorogenic probes. *J. Am. Chem. Soc.* **143**, 5674–5679 (2021).
30. Usama, S. M. et al. Targeted fluorogenic cyanine carbamates enable in vivo analysis of antibody–drug conjugate linker chemistry. *J. Am. Chem. Soc.* **143**, 21667–21675 (2021).
31. Miki, K. et al. pH-Responsive near-infrared fluorescent cyanine dyes for molecular imaging based on pH sensing. *Chem Comm* **53**, 7792–7795 (2017).
32. Oe, M. et al. pH-Responsive Cy5 dyes having nucleophilic substituents for molecular imaging. *Tetrahedron Lett.* **59**, 3317–3321 (2018).
33. Mu, H. et al. pH-Activatable cyanine dyes for selective tumor imaging using near-infrared fluorescence and photoacoustic modalities. *ACS Sens.* **6**, 123–129 (2021).
34. Oe, M., Miki, K., Masuda, A., Nogita, K. & Ohe, K. An activator-induced quencher-detachment-based turn-on probe with a cationic substrate moiety for acetylcholinesterase. *Chem. Commun.* **58**, 1510–1513 (2022).
35. Baldwin, J. Rules for ring closure. *J. Chem. Soc.* 734–736 (1976).
36. Uno, S. N. et al. A spontaneously blinking fluorophore based on intramolecular spirocyclization for live-cell super-resolution imaging. *Nat. Chem.* **6**, 681–689 (2014).
37. Hall, L. M., Gerowska, M. & Brown, T. A highly fluorescent DNA toolkit: synthesis and properties of oligonucleotides containing new Cy3, Cy5 and Cy3B monomers. *Nucleic Acids Res.* **40**, 1–10 (2012).
38. Wolf, N., Kersting, L., Herok, C., Mihm, C. & Seibel, J. High-yielding water-soluble asymmetric cyanine dyes for labeling applications. *J. Org. Chem.* **85**, 9751–9760 (2020).
39. Kim, I. K. & Erickson, K. L. Models for uleine-alkaloid biogenesis. *Tetrahedron* **27**, 3979–3991 (1971).
40. Wang, L. et al. Novel asymmetric Cy5 dyes: synthesis, photostabilities and high sensitivity in protein fluorescence labeling. *J. Photochem. Photobiolol. A* **210**, 168–172 (2010).
41. Frei, M. S. et al. Engineered HaloTag variants for fluorescence lifetime multiplexing. *Nat. Methods* **19**, 65–70 (2022).
42. Gautier, A. et al. An engineered protein tag for multiprotein labeling in living cells. *Chem. Biol.* **15**, 128–136 (2008).
43. Meng, G. et al. Modular click chemistry libraries for functional screens using a diazotizing reagent. *Nature* **574**, 86–89 (2019).
44. Pescitelli, G. & Bruhn, T. Good computational practice in the assignment of absolute configurations by TDDFT calculations of ECD spectra. *Chirality* **28**, 466–474 (2016).
45. Lukinavičius, G. et al. Fluorogenic probes for live-cell imaging of the cytoskeleton. *Nat. Methods* **11**, 731–733 (2014).
46. Belov, V. N. et al. Synthesis of fluorescent Jasplakinolide analogues for live-cell STED microscopy of actin. *J. Org. Chem.* **85**, 7267–7275 (2020).
47. Lukinavičius, G. et al. SiR–Hoechst is a far-red DNA stain for live-cell nanoscopy. *Nat. Commun.* **6**, 8497 (2015).
48. Cooper, M. et al. Cy3B™: improving the performance of cyanine dyes. *J. Fluoresc.* **14**, 145–150 (2004).
49. Oliinyk, O. S. et al. Deep-tissue SWIR imaging using rationally designed small red-shifted near-infrared fluorescent protein. *Nat. Methods* **20**, 70–74 (2023).
50. Ficken, G. E. & Kendall, J. D. The reactivity of the alkylthio-group in nitrogen ring compounds. Part II. Cyanine bases from 3,3-dimethyl-2-methylthio-3H-indole. *J. Chem. Soc.* 1529–1536 (1960).
51. Bandi, V. G. et al. Targeted multicolor in vivo imaging over 1,000 nm enabled by nonamethine cyanines. *Nat. Methods* **19**, 353–358 (2022).

Methods

General remarks

All reagents were purchased from commercial sources and used as received. Anhydrous solvents were procured from Acros Organics and used as received. Nuclear magnetic resonance spectra were acquired on a Bruker 400 or 600 instrument using TopSpin 4.2.0 and analysed with MestreNova 14.2. The ^{1}H NMR chemical shifts are reported in parts per million relative to $SiMe_4$ ($\delta = 0$) and were referenced internally with respect to residual protons in the solvent ($\delta = 7.26$ for $CDCl_3$, $\delta = 1.94$ for CD_3CN, $\delta = 3.31$ for CD_3OD, and $\delta = 2.50$ for $(CD_3)_2SO$). Coupling constants are reported in hertz. The ^{13}C NMR chemical shifts are reported in parts per million relative to $SiMe_4$ ($\delta = 0$) and were referenced internally with respect to solvent signal ($\delta = 77.16$ for $CDCl_3$, $\delta = 1.32$ for CD_3CN, $\delta = 49.00$ for CD_3OD and $\delta = 39.52$ for $(CD_3)_2SO$). High-resolution mass spectra were acquired on a timsTOF Pro TIMS-QTOF LC/MS spectrometer (Bruker Daltonics GmbH) by using electrospray ionization and analysed using Xcalibur v.4.2 software. IUPAC names of all compounds are provided and were determined using CS ChemBioDrawUltra v.16.0.

Computational modelling

All calculations were performed using Gaussian 09 at the B3LYP/DGTZVP level of theory as well as at the M06-2X/DGTZVP level. An implicit solvation model (IEFPCM) was used to simulate the effect of an aqueous environment. All stationary states were characterized by harmonic analysis at the same level of theory. All minima displayed zero imaginary frequencies and all transition states gave one imaginary frequency along the C–O bond elongation coordinate. Energies were corrected by zero-point energy.

Optical spectroscopy

Stock solutions were prepared in DMSO (spectrophotometric grade >99.9%) at concentrations of 5 mM, 1 mM and 50 µM and stored at −20 °C. Spectroscopic measurements were conducted in PBS. Ultraviolet–visible spectra were acquired using a Multiskan SkyHigh Microplate Spectrophotometer (ThermoFisher Scientific) and quartz cuvettes from ThorLabs (10 mm path length).

Buffered aqueous solutions in the pH range of 2 to 8 were prepared by mixing citric acid (0.1 M) and sodium dihydrogen phosphate NaH_2PO_4 (0.2 M) in ultrapure water. Buffered aqueous solutions in the pH range of 9 to 11 were prepared by mixing sodium bicarbonate (0.1 M) and sodium carbonate (0.1 M) in ultrapure water. Buffered aqueous solutions in the pH range of 12 to 13 were prepared by mixing potassium chloride KCl (0.2 M) and sodium hydroxide (0.2 M); 5 µM solutions of the dyes in the buffered aqueous solutions were prepared and the absorbance spectra were recorded after 1.5 h in triplicates using 96-well plates (Corning) on the MultiSkan SkyHigh microplate reader. The obtained ultraviolet–visible spectra were background corrected and the absorbance maxima of each pH value were normalized. Normalized absorbance values were plotted against the pH value and fitted (non-linear fit, sigmoidal, 4PL) using Prism 9.

Solutions of different dielectric constant were prepared by making water-dioxane mixtures containing 10% ($\varepsilon = 72.02$), 20% ($\varepsilon = 63.50$), 30% ($\varepsilon = 54.81$), 40% ($\varepsilon = 45.96$), 50% ($\varepsilon = 36.89$), 60% ($\varepsilon = 28.09$), 70% ($\varepsilon = 19.73$), 80% ($\varepsilon = 12.19$) or 90% ($\varepsilon = 6.23$) dioxane (by volume) in water[52].

We prepared 10 µM solutions of the dyes in the dioxane–water mixtures and the absorbance spectra were recorded in triplicates using 96-well plates (Corning) on a MultiSkan SkyHigh microplate reader. The obtained ultraviolet–visible spectra were background-corrected and the absorbance maxima of each dioxane-water mixture were normalized. Normalized absorbance values were plotted against the dielectric constant and fitted (non-linear fit, sigmoidal, 4PL) using Prism 9.

Extinction coefficients were obtained by measuring the absorbance spectra at various concentrations between 1 µM and 15 µM. The absorbance maxima were plotted against the corresponding concentration and fitted (simple linear regression) using Prism 9.

Fluorescence spectra were acquired using an FS5 Spectrofluorometer operated with Fluoracle software (Edinburgh Instruments) equipped with an SC-25 cuvette holder or SC-40 plate reader. Absolute fluorescence quantum yields were determined using 1 µM solutions employing an integrating sphere (SC-30, Edinburgh instruments). All spectroscopic measurements were performed in triplicate and at room temperature.

Photobleaching experiments were performed using a FS5 Spectrofluorometer equipped with an SC-25 cuvette holder. Protein adducts were measured at a 50 nM concentration and the emission slit width was adjusted individually for each dye to achieve a power of 1.2 mW (547 nm, 12 nm; 646 nm and 654 nm, 22.5 nm; 751 nm, 29.9 nm). The emission slit width was set to 0.75 nm and the fluorescence was measured every second for 10 min while keeping the shutter always open. The power was measured at the cuvette holder using a PMD100D compact power and energy meter console equipped with a S120VC standard photodiode power sensor (UV-Extended Si, 200–1,100 nm, 50 mW, Thorlabs GmbH).

Cloning

All plasmids were cloned by Gibson assembly. DNA encoding SNAPf or H2B-SNAPf was amplified from pSNAPf-H2B control plasmid (Addgene no. 101124) to generate an insert. To generate a backbone containing an organelle-specific targeting group and a fluorescent protein, the plasmids pmTurquoise2-ER (Addgene no. 36204) and pmTurquoise2-Golgi (Addgene no. 36205) were used. Primers for amplification (minimum 15 overlapping base pairs) were generated using SnapGene and modified manually to minimize secondary structures, self-dimers and repeated motifs. The designed primers were supplied by Microsynth AG (Switzerland) and are reported in Supplementary Tables 2 and 3. Vector and insert fragments were amplified by PCR using a Phusion High-Fidelity PCR Master Mix with HF buffer from New England Biolabs (NEB). The fragments were analysed by agarose gel electrophoresis and template DNA was digested using DpnI. PCR fragments were purified using a QIAquick PCR purification kit (Qiagen) according to the manufacturer's instructions. The Gibson assembly reaction was performed using the Gibson Assembly Master Mix (NEB) according to the manufacturer's protocol. DH5α competent *Escherichia coli* cells (NEB, C2987I) were transformed with the assembly product by heat shock following the manufacturer's instructions, streaked onto lysogeny broth (LB) agar plates containing kanamycin (50 µg ml^{-1}), and incubated at 37 °C for 24 h. Single colonies were selected and grown in LB liquid medium containing 50 µg ml^{-1} kanamycin at 37 °C for 16 h. Plasmid DNA was isolated using the QIAprep spin miniprep kit (Qiagen) according to the manufacturer's instructions. The correct sequence of the gene of interest was verified by the Sanger sequencing service of Microsynth using the standard sequencing primers CMV-F, SV40pA-R, and EGFP-C. All plasmids produced in this paper are available on Addgene (no. 197494–98).

Expression and purification of fSNAP protein

pET24b-6His-fSNAP (Addgene no. 106999) was transformed into *E. coli* strain Rosetta2(DE3) (Merck, 71397) and streaked on an agar plate with kanamycin and chloramphenicol resistance. A single colony was picked, inoculated in 80 ml LB cultures containing 50 µg ml^{-1} kanamycin and 25 µg ml^{-1} chloramphenicol, and grown at 37 °C for 24 h. We innoculated 40 ml of the starter culture into 4 l of medium and shaken at 37 °C to an optical density at 600 nm (OD_{600}) of 0.8. Expression was induced by the addition of 0.5 mM isopropyl β-D-thiogalactopyranoside, and cells were grown at 18 °C for 16 h. Cells were harvested by centrifugation, resuspended in HEPES buffer (300 mM NaCl, 20 mM HEPES, pH = 7.5), and supplemented with turbonuclease (20 µl) and a protease inhibitor cocktail tablet (Roche). Cells were lysed by sonication (70% power, 10 s pulse/10 s pulse off for 2 min, 30 s) and the lysate was cleared by centrifugation. The protein was purified by Ni-His-affinity column chromatography and the fractions were analysed by SDS–PAGE. The fractions

containing the protein were concentrated using Amicon Ultra-4 and Ultra-15 centrifugal filter units (MWCO 10 kDa) and further purified by size-exclusion chromatography. The correct size and purity of the protein were verified by SDS–PAGE analysis. Purified SNAP protein was stored in aliquots in a buffer containing 150 mM NaCl, 20 mM HEPES, pH 7.4, 1 mM DTT at −80 °C.

Protein-binding turn-on assays

Prior to biological assays with purified SNAP-tag protein, the buffer was exchanged to PBS using Zebra Spin Desalting Columns (Thermo Scientific) according to the manufacturer's protocol. SNAP-dyes (1 mM in DMSO) were either added to PBS alone or to a 5 μM SNAP-protein solution in PBS. The final concentration of SNAP-dyes was 2.5 μM and the resulting mixtures were incubated at 37 °C for 1.5 h.

The turn-on assay with actin was performed according to a published procedure[45]. Actin ligand **17**-actin (1 mM in DMSO) was added to either supplemented actin buffer alone or in the presence of 0.4 mg ml^{-1} G-actin (catalogue no. AKL99, Cytoskeleton). The final ligand concentration was 2.5 μM. The supplemented actin buffer contained 5 mM Tris-HCl pH 8.0, 0.2 mM $CaCl_2$ (from General Actin Buffer, catalogue no. BSA01, Cytoskeleton), 50 mM KCl, 2 mM $MgCl_2$, 5 mM guanidine carbonate and 1.2 mM ATP (from Actin Polymerization Buffer, catalogue no. BSA02, and ATP, catalogue no. BSA04, Cytoskeleton). Samples were incubated at 37 °C for 2 h.

The DNA-binding assay was performed according to a published procedure[47]. The hairpin-forming 28-bp DNA oligonucleotide was purchased from Microsynth (5′-CGCGAATTCGCGTTTTCGCGAATTCGCG-3′) and dissolved in Tris-buffered saline (TBS, 50 mM Tris-HCl, 150 mM NaCl, pH 7.4) at 1 mM concentration. The folding of the DNA into the secondary hairpin structure was achieved by heating the DNA at 75 °C for 2 min followed by slowly cooling to 25 °C. Nucleus ligand **18**-DNA (1 mM in DMSO) was incubated with either TBS (50 mM Tris-HCl, 150 mM NaCl, pH 7.4) alone or in the presence of 50 μM hairpin DNA at room temperature for 1 h. The final ligand concentration was 1 μM.

Absorbance spectra were recorded in 96-well plates (Corning) on the Multiskan SkyHigh microplate reader and fluorescence measurements were performed on the FS5 Spectrofluorometer (Edinburgh Instruments) equipped with a SC-40 plate holder. All spectroscopic measurements were carried out in triplicates and at room temperature.

Cell culture and fluorescence imaging

HeLa cells (CLS, 300194CP5) were grown in Dulbecco's Modified Eagle Medium supplemented with foetal bovine serum (10%) and penicillin-streptomycin (1%) at 37 °C in a 95% humidity atmosphere under a 5% CO_2 environment. The cells were grown to 90% confluency before seeding at a density of 15–20 000 cells per millilitre onto Ibidi μ-Slide 8-well glass-bottom plates 48 h before the imaging experiment. Cells were transfected with the plasmids H2B-SNAPf-mTurquoise2 (Addgene no. 197494), LifeAct-SNAPf-mTurquoise2 (no. 197497), TOM20-SNAPf-mTurquoise2 (no. 197496), SNAPf-mTurquoise2-KDEL (no. 197498) or SNAPf-mTurquoise2 (no. 197495) using jetPrime according to the manufacturer's protocol 24 h before imaging. Cells were incubated with the respective probes in FluoroBrite Dulbecco's Modified Eagle Medium for 1.5 h and imaged directly.

Confocal microscopy

Confocal imaging was performed with a Nikon W1 spinning disk microscope operated with NIS Elements AR software equipped with a CMOS camera (Photometrix). Brightfield imaging was performed with a white LED. Laser lines and filters were set up for the appropriate channel as described in Supplementary Table 5.

Images were collected using a CFI Plan Apochromat Lambda D oil immersion objective (60×, NA = 1.4). Channels were imaged sequentially. The microscope was operated using NIS Elements. Imaging experiments were performed at 37 °C in a 5% CO_2 environment. Images were analysed by Fiji/ImageJ.

Determination of the absolute configuration of (+)−6 and (−)−6

Circular dichroism spectra were measured with a Chirascan V100 CD spectrometer (Applied Photophysics) and operated using the Chirascan v.4.2 software. For circular dichroism measurements, 60 μM solutions of (+)-**6** and (−)-**6** in PBS were used. Optical rotation measurements were performed with a Jasco P-2000 polarimeter and operated using the Spectra Manager CFR software.

For TD-DFT calculations, we first performed a systematic conformational search at the B3LYP/DGTZVP level of theory with an implicit solvation model (IEFPCM) by varying all rotatable bonds in 60° steps. We then applied the Boltzmann distribution to the set of low-energy minima obtained by using the free energy differences, and considered the structures above the 0.1% population threshold for the TD-DFT calculation. Time-dependent density functional theory calculations were performed at the CAM-B3LYP/DGTZVP level of theory with IEFPCM as the solvation model.

Fluorescence lifetime imaging

Fluorescence lifetime imaging was performed on a Leica SP8 inverse FALCON confocal laser scanning microscope and operated using the Leica LAS X Navigator. Images were collected using an HC PL APO corr CS2 oil objective (63×, NA = 2.4) and the RHOD fluorescence filter set (excitation = 546/10, emission = 585/40). Phasor analysis of the FLIM data was performed with the Leica LAS X Phasor License.

Single-molecule localization microscopy

HeLa cells (CLS, 300194CP5) were transfected with β-tubulin-SNAP plasmid using jetPrime according to the manufacturer's protocol 48 h before imaging. Cells were incubated with probe **11** (100 nM) for 14 h, then detached and transferred to a new Ibidi slide. Cells were left for 10 h to adhere to the glass surface, and the medium was exchanged to FluoroBrite prior to imaging. Single-molecule imaging was performed on a Ti2 eclipse inverted microscope (Nikon) equipped with a water-cooled iXon 888 Ultra EMCCD camera (Andor) at 37 °C in a 5% CO_2 environment. Acquisitions were performed at 638 nm (90 mW, 30 ms) and a single band 708/75 emission filter was used. 2000 frames were acquired. Acquisitions were collected using a NIKON 100x TIRF Apo Plan SR oil objective (NA = 1.49). All laser and camera shutters were controlled by a NIDAQ oscilloscope (National Instruments) controller unit. The single-molecule signal was fitted with 2D Gaussian point spread functions using ThunderSTORM. The localization threshold was set to 1.1*std(Wave.F1).

Reporting summary

Further information on research design is available in the Nature Portfolio Reporting Summary linked to this article.

Data availability

All data supporting this paper, including coordinates for all calculated structures, are available through Zenodo[53]. X-ray crystallographic datasets used for modelling are available from the PDB under accession nos. 6Y8P and 1DNH. Samples of small-molecule probes are available from the authors on reasonable request. Source Data are provided with this paper.

References

52. Critchfield, F. E., Gibson, J. A. Jr. & Hall, J. L. Dielectric constant for the dioxane–water system from 20 to 35 °C. *J. Am. Chem. Soc.* **75**, 1991–1992 (1953).
53. Martin, A. & Rivera-Fuentes, P. *A General Strategy to Develop Fluorogenic Polymethine Dyes for Bioimaging* (Zenodo, 2023); https://doi.org/10.5281/zenodo.7588846

Acknowledgements
This work was supported by EPFL (SViPhD internal grant, P.R.-F.), University of Zurich, and the European Research Council (ERC Starting Grant HDPROBES no. 801572 to P. R.-F.). We thank S. Emmert for assistance with FLIM, L. Blatti (University of Zurich) for the synthesis of some indoleninium building blocks, K. Gademann for access to a polarimeter, and P. Gönczy and L. Reymond for valuable discussions. This work made use of infrastructure services provided by SCITAS, the Scientific IT and Application Support of EPFL, and the Service and Support for Science IT (S^3IT) at the University of Zurich. Samples of jasplakinolide and Hoechst 33342 ligands were donated by Spirochrome AG (https://spirochrome.com/). FLIM was performed at the Center for Microscopy and Image Analysis of the University of Zurich. The funders had no role in study design, data collection and analysis, decision to publish or preparation of the manuscript.

Author contributions
A.M. and P.R.-F. conceived the method, wrote the manuscript, perfomed computational modelling and analysed the results. A.M. performed all of the experiments. P. R.-F. acquired funding and supervised the project.

Competing interests
EPFL and University of Zurich jointly filed a patent application (EP23153834.9) protecting the invention disclosed in this paper. A. M. and P. R.-F. are listed as co-inventors.

Additional information
Extended data is available for this paper at https://doi.org/10.1038/s41557-023-01367-y.

Supplementary information The online version contains supplementary material available at https://doi.org/10.1038/s41557-023-01367-y.

Correspondence and requests for materials should be addressed to Pablo Rivera-Fuentes.

Peer review information *Nature Chemistry* thanks Kouichi Ohe, Francisco Raymo and the other, anonymous, reviewer(s) for their contribution to the peer review of this work.

https://doi.org/10.1038/s41557-023-01367-y

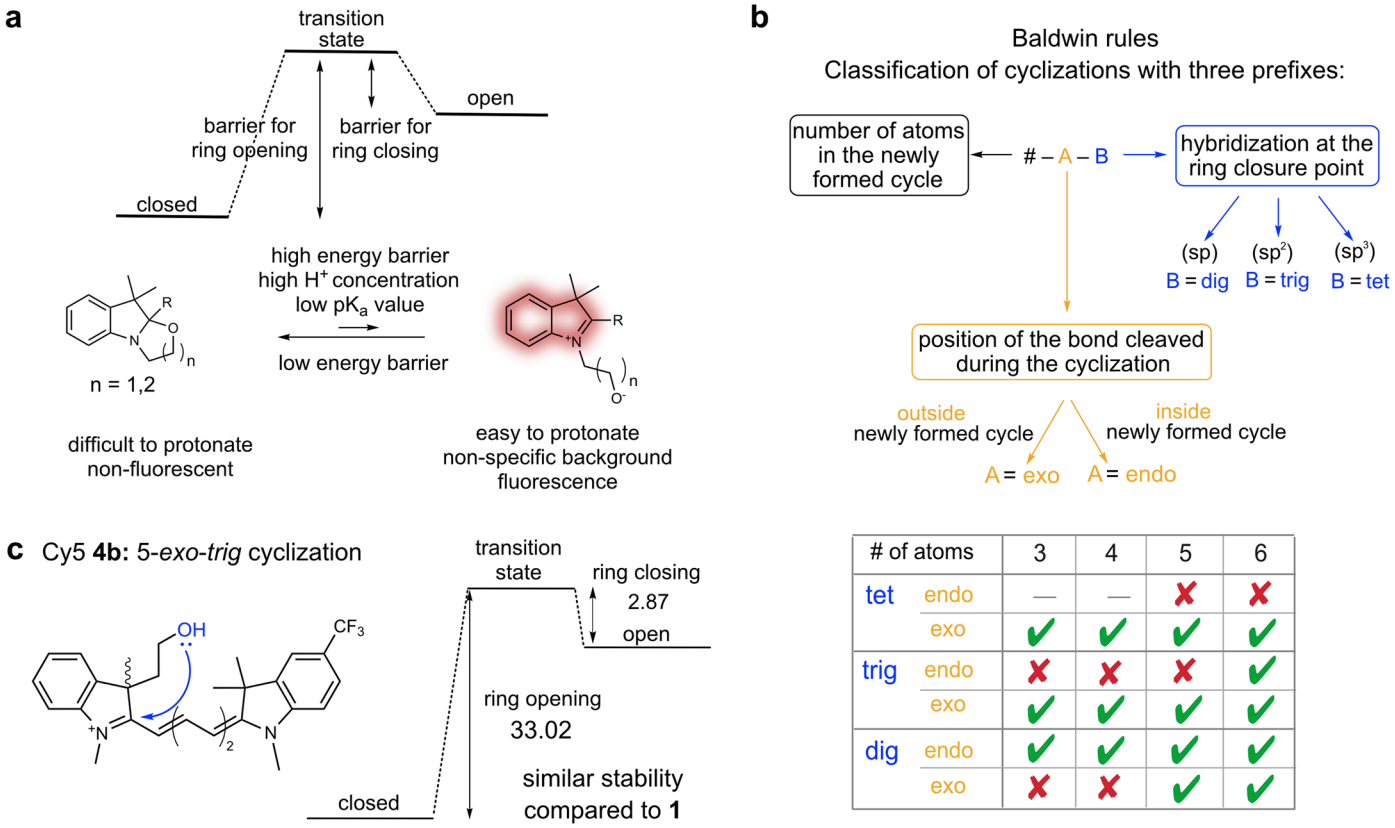

# of atoms		3	4	5	6
tet	endo	—	—	✘	✘
	exo	✔	✔	✔	✔
trig	endo	✘	✘	✘	✔
	exo	✔	✔	✔	✔
dig	endo	✔	✔	✔	✔
	exo	✘	✘	✔	✔

Extended Data Fig. 1 | Probe design and Baldwin rules. a) Cyclization energy landscape that favours fluorogenicity: A large barrier of ring opening and a small barrier of ring closure. **b**) Explanation of the Baldwin rules. **c**) Structure and calculated energy of ring opening and closing of Cy5 derivative **4b**. Calculations were carried out at the B3LYP/DGTZVP level of theory and energy values are reported in kcal mol^{-1}.

https://doi.org/10.1038/s41557-023-01367-y

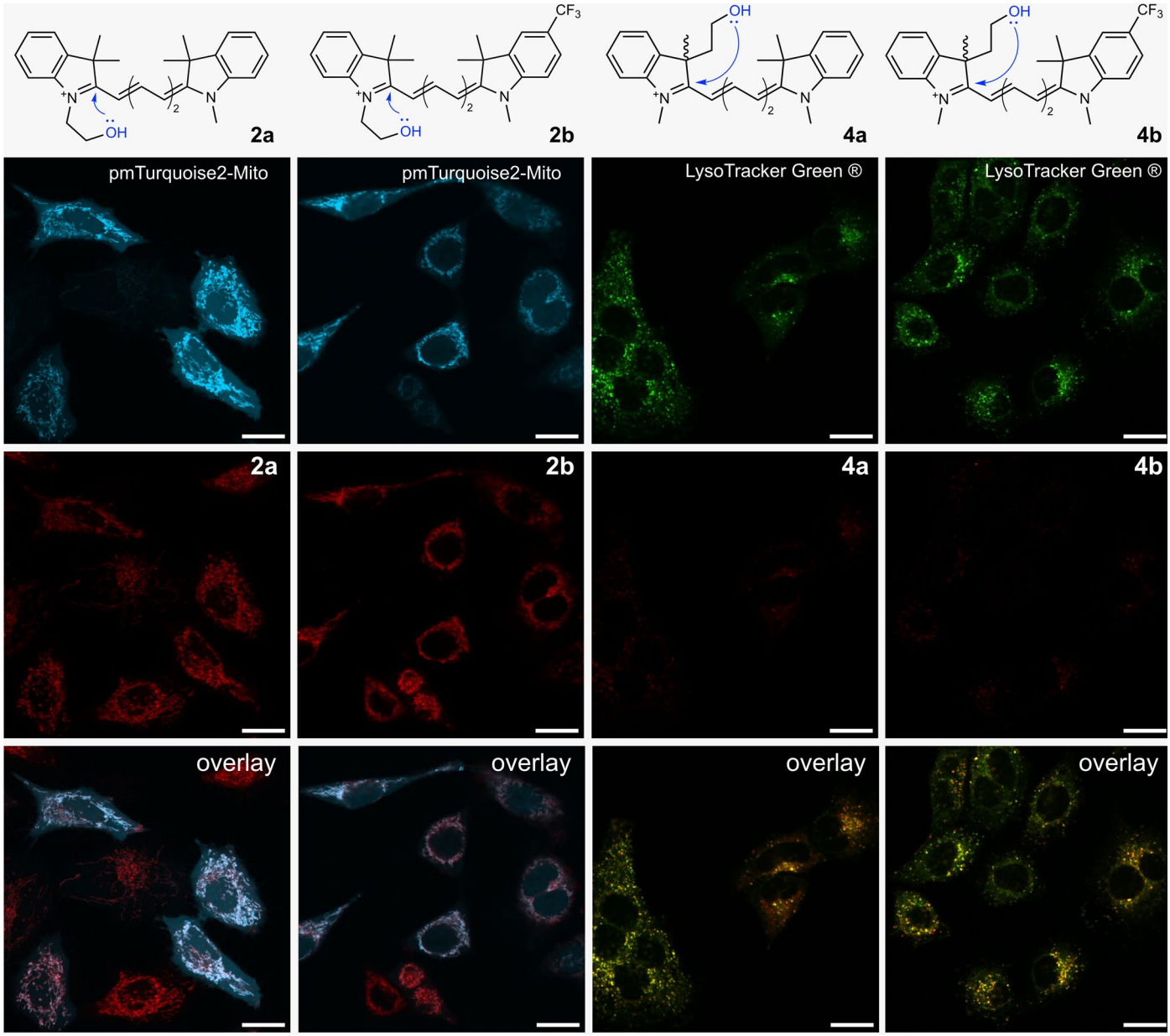

Extended Data Fig. 2 | Subcellular localization of untargeted dyes 2a, 2b, 4a, and 4b. For 5-*endo-trig* probes **2a** and **2b**, HeLa cells were transfected with a plasmid encoding for COX8A-mTurquoise2 and incubated with 250 nM **2a** or **2b** for 2 h. For 5-*exo-trig* probes **4a** and **4b**, HeLa cells were incubated with 250 nM **4a** or **4b** for 2 h. LysoTracker Green® (100 nM) was added 15 min prior to imaging. Scale bars: 15 µm. Micrographs are representative of three independent biological samples measured over three separate imaging sessions.

https://doi.org/10.1038/s41557-023-01367-y

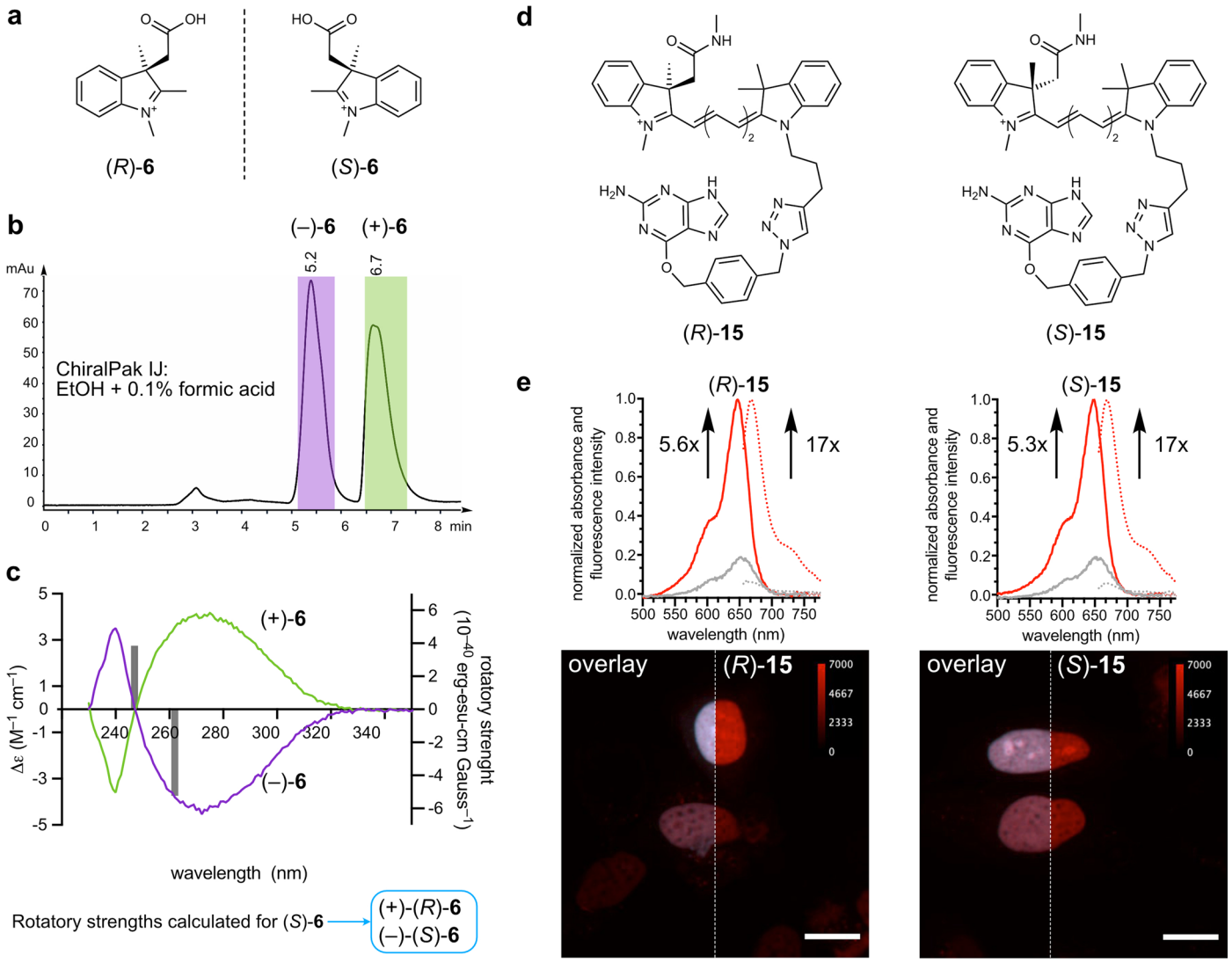

Extended Data Fig. 3 | Separation and evaluation of enantiomers (*S*)-15 and (*R*)-15. a) Structure of the enantiomers (*S*)-**6** and (*R*)-**6**. **b**) Separation of enantiomers (*S*)-**6** and (*R*)-**6** by HPLC under the conditions indicated. **c**) Determination of the absolute configuration of the enantiomers of **6** by electronic circular dichroism and comparison with the calculated rotatory strengths (grey bars) of (*S*)-**6** using TD-DFT (CAM-B3LYP/DGTZVP). Spectra were measured once. **d**) Structures of the enantiomeric dyes (*S*)-**15** and (*R*)-**15**. **e**) Protein-binding turn-on of probes (*S*)-**15** and (*R*)-**15** (2.5 µM) incubated with 5 µM purified SNAP-tag protein in PBS, pH 7.4, for 1.5 h. No-wash confocal microscopy of live HeLa cells transfected with H2B-SNAPf-mTurq2 and incubated with (*S*)-**15** (50 nM) and (*R*)-**15** (50 nM). Scale bars: 15 µm. Spectra are the mean of three independent experiments and micrographs are representative of three independent biological samples measured over three separate imaging sessions. Grey lines indicate absorbance (solid line) or fluorescence (dotted line) of the free dye in solution whereas coloured lines indicate absorbance (solid line) or fluorescence (dotted line) of the dye-protein conjugate.

https://doi.org/10.1038/s41557-023-01367-y

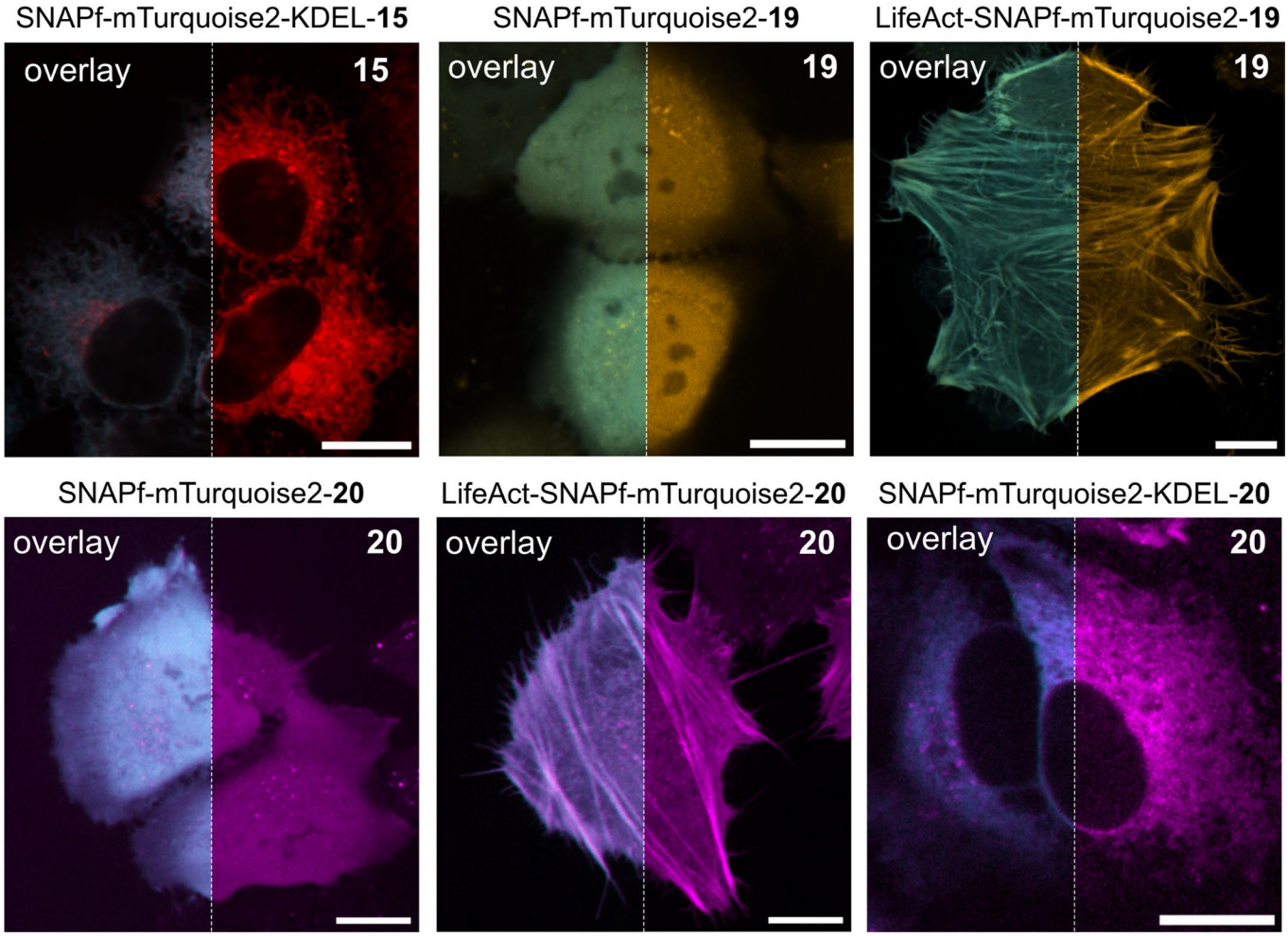

Extended Data Fig. 4 | Additional cellular targeting of probes 15, 19 and 20. No-wash confocal microscopy of live HeLa cells transfected with SNAPf-mTurquoise2-KDEL, SNAPf-mTurquoise2 or LifeAct-SNAPf-mTurquoise2 and incubated with **15** (50 nM), **19** (50 nM), or **20** (250 nM). The overlay shows the signal of the reference fluorescent protein mTurquoise2 and that of the indicated compound linked to SNAP-tag. Scale bars: 15 µm. Micrographs are representative of three independent biological samples measured over three separate imaging sessions.

nature portfolio

Corresponding author(s): Pablo Rivera-Fuentes

Last updated by author(s): Aug 8, 2023

Reporting Summary

Nature Portfolio wishes to improve the reproducibility of the work that we publish. This form provides structure for consistency and transparency in reporting. For further information on Nature Portfolio policies, see our Editorial Policies and the Editorial Policy Checklist.

Statistics

For all statistical analyses, confirm that the following items are present in the figure legend, table legend, main text, or Methods section.

n/a	Confirmed	
☐	☒	The exact sample size (*n*) for each experimental group/condition, given as a discrete number and unit of measurement
☐	☒	A statement on whether measurements were taken from distinct samples or whether the same sample was measured repeatedly
☒	☐	The statistical test(s) used AND whether they are one- or two-sided *Only common tests should be described solely by name; describe more complex techniques in the Methods section.*
☒	☐	A description of all covariates tested
☐	☒	A description of any assumptions or corrections, such as tests of normality and adjustment for multiple comparisons
☐	☒	A full description of the statistical parameters including central tendency (e.g. means) or other basic estimates (e.g. regression coefficient) AND variation (e.g. standard deviation) or associated estimates of uncertainty (e.g. confidence intervals)
☒	☐	For null hypothesis testing, the test statistic (e.g. *F*, *t*, *r*) with confidence intervals, effect sizes, degrees of freedom and *P* value noted *Give P values as exact values whenever suitable.*
☒	☐	For Bayesian analysis, information on the choice of priors and Markov chain Monte Carlo settings
☒	☐	For hierarchical and complex designs, identification of the appropriate level for tests and full reporting of outcomes
☒	☐	Estimates of effect sizes (e.g. Cohen's *d*, Pearson's *r*), indicating how they were calculated

Our web collection on statistics for biologists contains articles on many of the points above.

Software and code

Policy information about availability of computer code

Data collection	Xcalibur 4.2 (Thermo, mass spectrometry), TopSpin 4.2.0 (Bruker, NMR), Fluoracle (Edinburgh Instruments, fluorescence and absorbance), NIS elements AR (Nikon, microscopy), LAS X (Leica, FLIM), Chirascan 4.2 (Circular dichroism), Spectra Manager CFR (polarimatery), Leica LAS X Navigator (FLIM).
Data analysis	MestreNova 14.2 (mass spectrometry and NMR), Prism 9 (optical spectroscopy), Fiji (confocal and SMLM), LAS X Phasor (Leica, FLIM), ThunderSTORM 1.3 (SMLM)

For manuscripts utilizing custom algorithms or software that are central to the research but not yet described in published literature, software must be made available to editors and reviewers. We strongly encourage code deposition in a community repository (e.g. GitHub). See the Nature Portfolio guidelines for submitting code & software for further information.

Data

Policy information about availability of data

All manuscripts must include a data availability statement. This statement should provide the following information, where applicable:

- Accession codes, unique identifiers, or web links for publicly available datasets
- A description of any restrictions on data availability
- For clinical datasets or third party data, please ensure that the statement adheres to our policy

All data supporting this paper, including coordinates for all calculated structures, are available through Zenodo (DOI: 10.5281/zenodo.7588846). X-ray

crystallographic datasets used for modeling are available from the PDB under accession numbers 6Y8P and 1DNH. Source data are provided with this paper. Samples of small-molecule probes are available from the authors upon reasonable request.

Human research participants

Policy information about studies involving human research participants and Sex and Gender in Research.

Reporting on sex and gender	N/A
Population characteristics	N/A
Recruitment	N/A
Ethics oversight	N/A

Note that full information on the approval of the study protocol must also be provided in the manuscript.

Field-specific reporting

Please select the one below that is the best fit for your research. If you are not sure, read the appropriate sections before making your selection.

☒ Life sciences ☐ Behavioural & social sciences ☐ Ecological, evolutionary & environmental sciences

For a reference copy of the document with all sections, see nature.com/documents/nr-reporting-summary-flat.pdf

Life sciences study design

All studies must disclose on these points even when the disclosure is negative.

Sample size	No sample-size calculation was performed because no experiments in this paper were aimed at describing the properties of a population based on a subsample. In other words, all measurements presented in this paper are discussed independently with no assumption that any specific effect exists or there is a null hypothesis to be rejected. Thus, we do not compare effect sizes or discuss the statistical significance of any observed effects.
Data exclusions	For microscopy studies, dead cells (as judged by cell morphology and excesive blebbing) were excluded from analysis. No other data were excluded.
Replication	Optical spectroscopic measurements (UV and fluorescence) were repeated three times with samples that were prepared from independent batches of the molecule, diluted in independent batches of buffer or solvent, and measured independently. Live-cell experiments were carried out using three different batches of cells (independently cultured from different passage numbers) and measured on different imaging sessions (usually on different days). In all cases, the results of all replicates were virtually identical.
Randomization	No specific randomization strategy was followed. For microscopy studies, cells from different passage numbers were considered different experimental groups. For spectroscopic measurements, separate batches of small molecule or protein were considered independent samples.
Blinding	Blinding was not necessary because all imaging results were obtained using automated computational analysis, thus the researcher cannot affect the results. For all other experiments, group allocation was predetermined by the existence of specific batches of compounds or protein and the experimenter had no influence over the potential variability between groups.

Reporting for specific materials, systems and methods

We require information from authors about some types of materials, experimental systems and methods used in many studies. Here, indicate whether each material, system or method listed is relevant to your study. If you are not sure if a list item applies to your research, read the appropriate section before selecting a response.

Materials & experimental systems

n/a	Involved in the study
☒	☐ Antibodies
☐	☒ Eukaryotic cell lines
☒	☐ Palaeontology and archaeology
☒	☐ Animals and other organisms
☒	☐ Clinical data
☒	☐ Dual use research of concern

Methods

n/a	Involved in the study
☒	☐ ChIP-seq
☒	☐ Flow cytometry
☒	☐ MRI-based neuroimaging

Eukaryotic cell lines

Policy information about cell lines and Sex and Gender in Research

Cell line source(s)	HeLa (CLS 300194CP5)
Authentication	Cells were used as received from the distributor (CLS) without further authentication
Mycoplasma contamination	Cells were not tested for mycoplasma contamination
Commonly misidentified lines (See ICLAC register)	No commonly misidentified cell lines were used in this study.